PAPER

Check for updates

Doping and phase segregation in Mn^{2+}- and Co^{2+}-doped lead halide perovskites from ^{133}Cs and ^1H NMR relaxation enhancement†

Dominik J. Kubicki, [ID] [ab] Daniel Prochowicz, [ID] [bc] Arthur Pinon, [a] Gabriele Stevanato, [a] Albert Hofstetter, [a] Shaik M. Zakeeruddin, [ID] [b] Michael Grätzel*[b] and Lyndon Emsley [ID] *[a]

Lead halide perovskites belong to a broad class of compounds with appealing optoelectronic and photovoltaic properties. Doping with transition metal ions such as Mn^{2+} and Co^{2+} has recently been reported to substantially enhance luminescence and stability of these materials. However, so far atomic-level evidence for incorporation of the dopants into perovskite phases has been missing. Here, we introduce a general and straightforward method for confirming the substitutional doping of bulk perovskite phases with paramagnetic dopants. Using ^{133}Cs and ^1H solid-state MAS NMR relaxation measurements we provide for the first time direct evidence that, consistent with current understanding, Mn^{2+} is incorporated into the perovskite lattice of $CsPbCl_3$ and $CsPbBr_3$ and does not form clusters. We also show that, contrary to current conviction, Co^{2+} is not incorporated into the perovskite lattice of $MAPbI_3$.

Introduction

Lead halide perovskites are highly promising semiconducting materials for optoelectronic and photovoltaic applications.[1] All-inorganic cesium lead halide ($CsPbX_3$, X = Cl, Br, I) nanocrystals have recently emerged as a viable alternative to classical II–VI metal chalcogenides used in LED and solar cell applications.[2–6] Similarly, multi-component organic–inorganic lead halide perovskites ($APbX_3$, A = methylammonium ($CH_3NH_3^+$, MA), formamidinium ($CH_3(NH_2)_2^+$, FA), (X = Cl, Br, I)) applied as light absorbers in solar cells, currently provide power conversion efficiencies of over 22%.[7,8]

All-inorganic lead halide perovskite quantum dots (QDs) doped with transition metal and lanthanide ions show particularly advantageous optoelectronic properties such as strongly sensitized luminescence[9,10] and improved thermal and air stability.[11,12] The most widely investigated materials are $CsPbCl_3$,[10,13–22] $CsPbBr_3$,[23–26] and $CsPbI_3$[9,12] as well as mixed-halide compositions[10,27–29] doped with Mn^{2+} and very recently

[a]Laboratory of Magnetic Resonance, Institute of Chemical Sciences and Engineering, Ecole Polytechnique Fédérale de Lausanne (EPFL), CH-1015 Lausanne, Switzerland. E-mail: lyndon.emsley@epfl.ch

[b]Laboratory of Photonics and Interfaces, Institute of Chemical Sciences and Engineering, Ecole Polytechnique Fédérale de Lausanne (EPFL), CH-1015 Lausanne, Switzerland. E-mail: michael.graetzel@epfl.ch

[c]Institute of Physical Chemistry, Polish Academy of Sciences, Kasprzaka 44/52, 01-224 Warsaw, Poland

† Electronic supplementary information (ESI) available. See DOI: 10.1039/c8ta11457a

Ce^{3+}.[30] The strategy of transition metal ion doping has also been proposed as a means of fine tuning of photovoltaic parameters in organic–inorganic lead halide perovskites.[31,32] Incorporation of transition metal ions into the perovskite lattice is typically evidenced using XRD, UV-VIS, PL, and in some instances by EPR[10,11,18] and HAADF-STEM.[11,30,33] While some of these methods provide atomic-level resolution (HAADF-STEM, EPR) and others provide insight into phase composition (XRD), none of them achieves both. Cesium lead halides form a variety of non-perovskite phases with different stoichiometries[34–36] but there are currently no experimental protocols that can confirm which phase of interest is doped with transition metals. On the other hand, NMR is capable of providing atomic-level resolution by utilizing local nuclear probes such as ^1H, ^{13}C, ^{14}N, ^{133}Cs, ^{87}Rb, ^{39}K and ^{207}Pb.[37–45] In particular, ^{207}Pb is a good probe of the halide composition[38] but is far less sensitive to other changes in composition.[46,47] Solid-state NMR spectra are acquired by placing a powder sample inside a strong homogeneous magnetic field (typically between around 10 and 20 T) and then recording spectra of the transitions between nuclear spin states which occur in the radiofrequency region. The resulting spectra contain peaks at distinct frequencies for each type of nucleus, and where very small variations (so-called chemical shifts) within a given nucleus type report very precisely on the local chemical environments of the nucleus in all its chemically inequivalent sites. For solids, the sample is usually rapidly spun at the magic angle (54.7° with respect to the magnetic field), which yields a very significant improvement in spectral resolution. This makes magic angle spinning (MAS)

2326 | *J. Mater. Chem. A*, 2019, 7, 2326–2333

This journal is © The Royal Society of Chemistry 2019

NMR one of the most powerful tools available to probe the local atomic-level structure of solids.[48]

Spectra are obtained from Fourier transformation of time domain signals recorded after a radiofrequency pulse that perturbs the system from equilibrium. The return to equilibrium after excitation by the pulse is referred to as longitudinal relaxation. Most transition metal and lanthanide ions are paramagnetic and therefore are expected to induce large paramagnetic relaxation enhancements (PRE) in otherwise diamagnetic perovskite materials.[49] PREs arise as a consequence of the electron spin-nuclear spin interactions between NMR active nuclei (e.g. ^{133}Cs or ^{1}H) and unpaired electrons of the metal ion, and lead to significant (up to 3–4 orders of magnitude) shortening of longitudinal relaxation times, T_1, of nuclei in close proximity to paramagnetic centers. PRE is a short-range effect and scales as $1/r$,[6] where r is the distance between the nucleus and the paramagnetic species, and typically can be observed for distances up to ~20 Å from the unpaired electron. The sensitivity limit for the detection of PREs is on the order of 0.1 s^{-1}.[50] In solids, another process, known as spin diffusion (SD)[51] can transport the magnetization to nuclei farther away from the paramagnetic centres, leading to substantially shorter apparent T_1 in the bulk of the material.

Here, using solid-state NMR relaxation measurements we provide for the first time atomic-level evidence that Mn^{2+} can dope CsPbCl$_3$ and CsPbBr$_3$ perovskite phases, consistent with replacing Pb^{2+} on the B site. We also show that, contrary to current belief, Co^{2+} is not capable of doping MAPbI$_3$. Our study establishes a straightforward and general method for confirming incorporation of paramagnetic dopants into perovskite lattices.

Experimental

Materials

The following materials were used: methylammonium iodide (DyeSol), PbI$_2$ (TCI, 99.99%), PbBr$_2$ (TCI), PbCl$_2$ (TCI), CsBr (Sigma, 99.999%), CsCl (Sigma, 99.999%), CoI$_2$ (abcr, 99.999%), MnBr$_2$ (abcr, 99%, anhydrous), MnCl$_2$ (abcr, 99.999%, ultra dry).

Perovskite mechanosynthesis

Starting materials were stored inside a glove box under argon. Perovskite powders were synthesized by grinding the reactants in an electric ball mill (Retsch Ball Mill MM-200) using a grinding jar (10 ml) and a ball (Ø 10 mm) for 30 min. at 25 Hz. The resulting perovskite powders were annealed at 250 °C for 10 minutes. The amounts of reagents taken into the synthesis were as follows: CsPbBr$_3$: 212.8 mg CsBr (1 mmol), 367.0 mg PbBr$_2$ (1 mmol), CsPb$_{0.995}$Mn$_{0.005}$Br$_3$: 212.8 mg CsBr (1 mmol), 1.1 mg MnBr$_2$ (0.005 mmol) 365.2 mg PbBr$_2$ (0.995 mmol), CsPb$_{0.97}$-Mn$_{0.03}$Br$_3$: 212.8 mg CsBr (1 mmol), 6.4 mg MnBr$_2$ (0.03 mmol) 356.0 mg PbBr$_2$ (0.97 mmol), CsPb$_{0.92}$Mn$_{0.08}$Br$_3$: 212.8 mg CsBr (1 mmol), 17.2 mg MnBr$_2$ (0.08 mmol) 337.6 mg PbBr$_2$ (0.92 mmol), CsMnBr$_3$: 212.8 mg CsBr (1 mmol), 214.8 mg MnBr$_2$ (1 mmol), CsPbCl$_3$: 168.4 mg CsCl (1 mmol), 278.0 mg PbCl$_2$ (1

mmol), CsPb$_{0.97}$Mn$_{0.03}$Cl$_3$: 168.4 mg CsCl (1 mmol), 3.8 mg MnCl$_2$ (0.03 mmol) 269.7 mg PbCl$_2$ (0.97 mmol), CsMnCl$_3$: 168.4 mg CsCl (1 mmol), 125.8 mg MnCl$_2$ (1 mmol), MAPbI$_3$: 159.0 mg MAI (1 mmol), 461.0 mg PbI$_2$ (1 mmol), MA$_2$CoI$_4$: 318.0 mg MAI (2 mmol), 312.7 mg CoI$_2$ (1 mmol), MAPb$_{0.97}$-Co$_{0.03}$I$_3$: 159.0 mg MAI (1 mmol), 9.4 mg CoI$_2$ (0.03 mmol), 447.1 mg PbI$_2$ (0.97 mmol).

NMR measurements

Solid-state MAS NMR spectra of ^{1}H (900 MHz at 21.1 T) and ^{133}Cs (52.5 MHz at 9.4 T), were recorded on Avance IV 21.1 T and Bruker Avance III 9.4 T spectrometers, respectively, equipped with 3.2 mm CPMAS probes. Solid samples were packed into 3.2 mm diameter zirconia rotors and closed off using Vespel caps. The samples were spun at 20 kHz MAS (unless stated otherwise) using dry nitrogen gas. The rotation rate was controlled using a PID controller and its stability was ±1 Hz. Radiofrequency (RF) field strengths were calibrated directly on the samples of interest by acquiring an on-resonance nutation curve. ^{1}H chemical shifts were referenced to solid adamantane (δ = 1.91 ppm). ^{133}Cs shifts were referenced to 1 M aqueous solutions of cesium chloride, using solid CsI (δ = 271.05 ppm) as a secondary reference.[52] For the saturation-recovery experiments, saturation was achieved by applying a train of 30 π/2 pulses spaced by 3 ms.

Results and discussion

Fig. 1 schematically shows how paramagnetic metal ions can be incorporated into perovskite lattices. Analysis of XRD and TEM
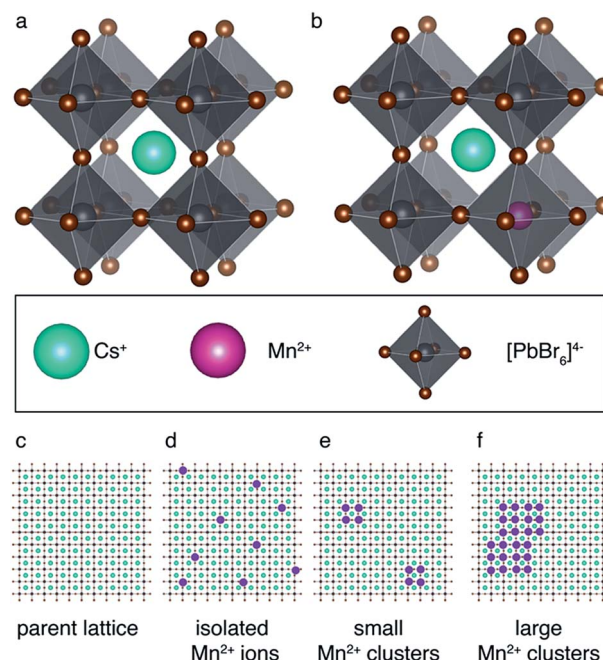

Fig. 1 Schematic representation of paramagnetic doping in perovskites: (a) parent CsPbBr$_3$ lattice, (b) homovalent B-site replacement. Schematic representation of possible scenarios for Mn^{2+} aggregation inside the perovskite lattice: (c) parent perovskite lattice, (d) isolated Mn^{2+} ions, (e) small Mn^{2+} clusters, (f) large Mn^{2+} clusters.

This journal is © The Royal Society of Chemistry 2019

J. Mater. Chem. A, 2019, 7, 2326–2333 | **2327**

data of Mn^{2+}-doped cesium lead halides has suggested lattice contraction consistent with homovalent B-site substitution (ionic radii: Pb^{2+}: 133 pm, Mn^{2+}: 97 pm).[9,11] Heterovalent A-site replacement with concomitant formation of A-site vacancies has never been considered as highly unlikely owing to even larger mismatch of ionic radii (Cs^{+}: 167 pm). In our analysis, we assume that homovalent B-site substitution is the dominant substitution mechanism. Since the Cs–Pb distance in the parent $CsPbBr_3$ lattice (Fig. 1a) is about 5 Å, replacing Pb^{2+} by Mn^{2+} is expected to cause substantial PRE. An important question associated with manganese doping is whether or not it is uniformly dispersed inside the perovskite lattice (Fig. 1c and d) or whether it forms larger manganese-rich domains (Fig. 1e and f). Since sensitised luminescence relies on the exchange of energy between the host lattice and the dopant, it is crucial to know if the dopant forms large aggregates. To answer these questions, we carried out ^{133}Cs relaxation measurements on mechanochemically[53,54] synthesized $CsPbBr_3$ undoped and stoichiometrically doped with 0.5, 3 and 8 mol% of Mn^{2+} (see Fig. S4† for the ^{133}Cs spectra). The corresponding saturation-recovery curves (Fig. 2a) show significantly faster recovery (shorter T_1) of ^{133}Cs nuclei in the perovskite phase of the Mn^{2+}-doped samples and indicate incorporation of the paramagnetic dopant into the perovskite lattice.

Since paramagnetic doping leads to a distribution of apparent relaxation times, the curves are best fitted using a stretched exponential function:

$$I(\tau) = y_0 + Ae^{-\left(\frac{\tau}{T_1}\right)^{\beta}} \qquad (1)$$

where $I(\tau)$ is the NMR signal intensity measured after τ seconds of recovery, y_0 is an offset accounting for imperfect saturation, T_1 is the relaxation time and β is the stretching factor. Undoped $CsPbBr_3$ has a ^{133}Cs T_1 of (109 ± 1) s with $\beta = 1$, indicating that its recovery is best described by a simple mono-exponential function (Table 1). This result is expected since all ^{133}Cs environments in this phase are identical and therefore should exhibit the same relaxation behaviour (discounting surface and lattice defects). We also note that quadrupolar spin-lattice relaxation is, in principle, multi-exponential in spinning powders but in practice departures from mono-exponential behaviour in compounds with symmetric coordination are very small.[55] Mn^{2+} doping causes significant shortening of the ^{133}Cs T_1 along with pronounced stretching to produce T_1s of about 4, 0.7 and 0.5 s with $\beta = 0.58, 0.54, 0.57$ for 0.5, 3 and 8% Mn^{2+}, respectively (Table 1). A stretching parameter less than 1 indicates the presence of a distribution of relaxation times, with cesium nuclei closest to the paramagnetic impurity being relaxed most efficiently. *This result directly evidences Mn^{2+} incorporation into the perovskite structure.* We note that the parameter β can take on values between 0.5 and 1, the different cases being thoroughly described in the literature.[56–61] Beside the case of $\beta = 1$ described above, the other limiting case of $\beta = 0.5$ has been theoretically justified for a random distribution of paramagnetic dopants when spin diffusion is absent.[57–59] Intermediate $0.5 < \beta < 1$ values were observed in a number of cases.[60,62] In our case, $\beta = 1$ corresponds to either fully
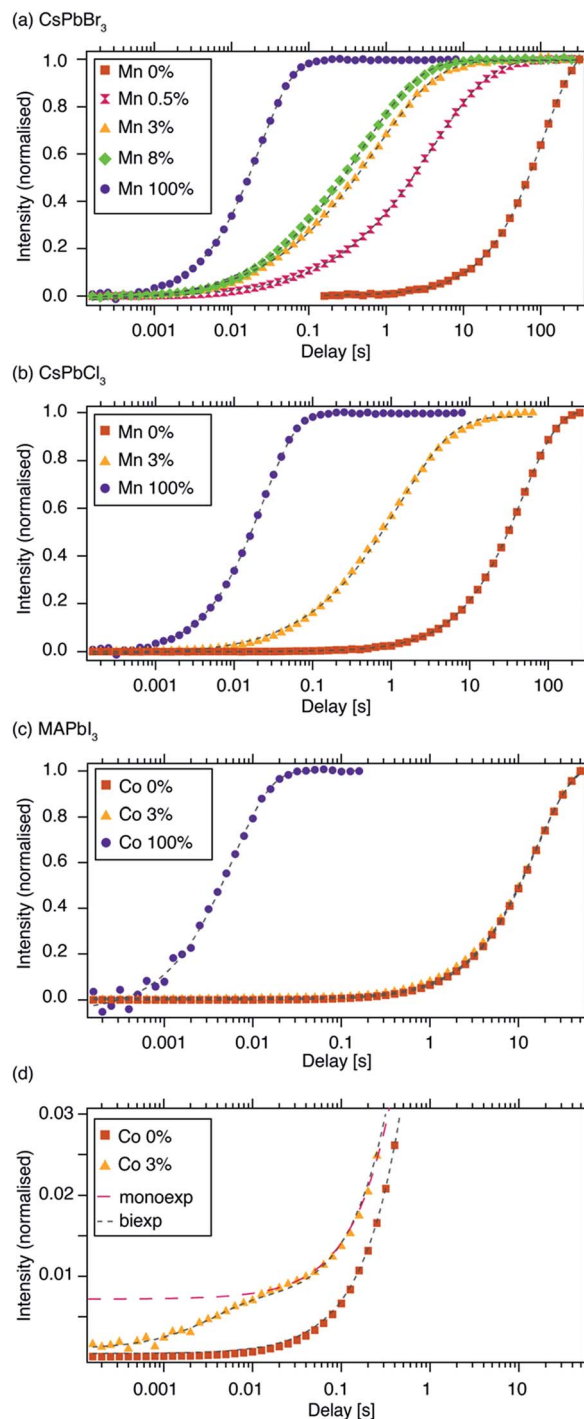

Fig. 2 ^{133}Cs T_1 build-up curves measured using a saturation-recovery sequence (shorthand legend labels are given in parentheses): (a) $CsPbBr_3$, ("Mn 0%") $CsPb_{0.995}Mn_{0.005}Br_3$ ("Mn 0.5%"), $CsPb_{0.97}Mn_{0.03}Br_3$ ("Mn 3%"), $CsPb_{0.92}Mn_{0.08}Br_3$ ("Mn 8%") and $CsMnBr_3$ ("Mn 100%"), (b) ^{133}Cs T_1 of $CsPbCl_3$, ("Mn 0%") $CsPb_{0.97}Mn_{0.03}Cl_3$ ("Mn 3%") and $CsMnCl_3$ ("Mn 100%"), (c) ^{1}H T_1 of $MAPbI_3$, ("Co 0%"), $MAPb_{0.97}Co_{0.03}I_3$ ("Co 3%") and MA_2CoI_4 ("Co 100%"), (d) a vertical zoom of the initial recovery period from panel "c". Experimental conditions: (a, b) at 9.4 T and 20 kHz MAS, (c) at 21.1 T and 20 kHz MAS. Dashed lines are fits: (a, b) stretched exponential, (c, d) mono-exponential (Co 0%, Co 100%), bi-exponential (black marker, Co 3%), mono-exponential (red marker, Co 3%). The curves were normalized to the fully recovered intensity. Raw data are given in the ESI.†

2328 | *J. Mater. Chem. A*, 2019, **7**, 2326–2333

This journal is © The Royal Society of Chemistry 2019

Table 1 ^{133}Cs T_1 relaxation times of Mn^{2+}-doped $CsPbBr_3$ and $CsPbCl_3$ fitted using the stretched exponential function. The reported errors correspond to one standard deviation in the precision of the fit

Material	^{133}Cs T_1 [s]	Stretching parameter β
$CsPbBr_3$	109 ± 1	0.999 ± 0.007
$CsPb_{0.995}Mn_{0.005}Br_3$	4.00 ± 0.02	0.585 ± 0.002
$CsPb_{0.97}Mn_{0.03}Br_3$	0.73 ± 0.01	0.541 ± 0.006
$CsPb_{0.92}Mn_{0.08}Br_3$	0.49 ± 0.01	0.569 ± 0.006
$CsMnBr_3$	0.0233 ± 0.0001	1.000 ± 0.009
$CsPbCl_3$	45.9 ± 0.1	0.941 ± 0.002
$CsPb_{0.97}Mn_{0.03}Cl_3$	1.27 ± 0.02	0.633 ± 0.008
$CsMnCl_3$	0.0388 ± 0.0002	0.976 ± 0.005

diamagnetic (no PREs) or strongly paramagnetic (manganese- and cobalt-rich) samples. Intermediate values of β correspond to doped samples which exhibit a distribution of T_1 values. For completeness, we also show data of a purely paramagnetic $CsMnBr_3$ with the antiperovskite structure.[63] In this case the ^{133}Cs T_1 is about 23 ms and $\beta = 1$, again consistent with no distribution of relaxation times since all ^{133}Cs are in direct contact with the paramagnetic species. We carried out analogous analysis for $CsPbCl_3$ doped with 3 mol% Mn^{2+} and confirmed that also in this case the paramagnetic dopant is incorporated into the perovskite phase (Fig. 2b). The EPR spectra of the Mn^{2+} doped materials as well as those of the reference paramagnetic phases are shown in Fig. S6.† For low doping ratios they show a set of six hyperfine components which become broadened as the manganese doping level increases. For $CsPb_{0.97}Mn_{0.03}Cl_3$ the hyperfine splitting is well resolved and its fitted value is $A_{iso}(^{55}Mn) = (241 \pm 1)$ MHz, consistent with typical Mn^{2+} hyperfine couplings in octahedral coordination.[64] The XRD patterns of the materials are shown in Fig. S1 (bromides) and S2† (chlorides). Finally, we note that analogous PRE effects are to be expected in ^{207}Pb NMR. However, longitudinal relaxation rates in lead halide perovskites under MAS are on the order of 100 ms (ref. 38 and [65]) which leaves little room for the detection of PREs. As regards the NMR of halogens, ^{127}I, $^{35/37}Cl$ and $^{79/81}Br$ are sensitive quadrupolar nuclei with a relatively large quadrupole moment, and therefore the line widths of the corresponding NMR spectra strongly depend on the symmetry of their local nuclear environment. In the case of lead halide perovskites, this translates to extremely wide spectra which are impractical to acquire.[42,66,67] In addition, owing to the efficient quadrupolar relaxation, the corresponding longitudinal relaxation times are typically below 1 s, leaving little room for PREs to operate.[68–70] On the other hand, ^{19}F is a spin 1/2 with relatively long longitudinal relaxation times which makes it perfectly suited for the task of detecting PREs.

B-site Co^{2+} incorporation has recently been reported and its effects studied for $MAPbI_3$, the widely used standard photovoltaic material.[34,48] Fig. 2c shows ^1H saturation-recovery curves of $MAPbI_3$ undoped and stoichiometrically doped with 3 mol% Co^{2+}, corresponding to the composition "$MAPb_{0.97}Co_{0.03}I_3$", that is assuming homovalent replacement of Pb^{2+} with Co^{2+}. High-spin cobalt(II) in octahedral (O_h) symmetry at a distance of

5 angstroms from a proton is expected to lead to ^1H PRE on the order of 30 s^{-1}, or more if the symmetry is lower.[50] The relaxation behaviour observed here is significantly different from the previous cases. ^1H T_1 relaxation of undoped $MAPbI_3$ is best described using a mono-exponential function with a T_1 of (15.89 ± 0.04) s (Table 2). Upon doping with Co^{2+}, no stretching is observed. Instead, a clear biexponential behaviour is evident (Fig. 2d), and a satisfactory fit is obtained by constraining the slowly relaxing component using the T_1 of the reference diamagnetic $MAPbI_3$ phase while fitting the small, fast relaxing component. This procedure yields a T_1 of (10 ± 10) ms for the fast relaxing component, with the large error being due to the very large intensity difference between the two components. This suggests the presence of undoped $MAPbI_3$ and a separate, purely paramagnetic phase (Fig. 2d). A mono-exponential fit yields a T_1 of (15.3 ± 0.2) s and does not provide a satisfactory description of the early phase of the recovery, as shown in Fig. 2d in the trace labelled "monoexp". The reference paramagnetic phase, MA_2CoI_4, has a T_1 of (6.7 ± 0.1) ms. *The clear biexponential relaxation behaviour and no shortening of T_1 of the $MAPbI_3$ perovskite phase provides compelling evidence that in this case Co^{2+} is not incorporated into the perovskite lattice.* We note that, in principle, the two components could be quantified to give the relative amounts of the two phases. However, since the T_1 measurements were carried out using an echo saturation-recovery sequence to remove the probe background, a sizeable portion of the cobalt-rich phase loses spin coherence due to fast T_2 relaxation during the 0.2 ms echo delay,[71–73] which in turn makes its signal intensity lower. On the other hand, the diamagnetic phase has a comparatively long T'_2, hence its coherence decays less in the spin echo experiment. The difference in coherence lifetimes of protons in the two phases makes the quantification of these saturation-recovery curves unreliable, as it underestimates the amount of the cobalt-rich phase. Using numerical simulations (*vide infra*), we demonstrate that the bi-exponential behaviour corresponds to the formation of cobalt-rich phases with a radius larger than 100 nm (see the ESI† for details).

We corroborate this result by comparing the ^1H, ^{13}C and ^{14}N MAS NMR spectra of the two materials (Fig. 4). The ^1H (Fig. 3a) and ^{13}C (Fig. 3b) isotropic chemical shifts as well as the ^{14}N shift (Fig. 3c and d) are, to within error, identical for both materials. The presence of paramagnetic ions should lead to hyperfine shifts of the neighbouring nuclei. For protons at a distance of 5 angstroms from a high-spin Co^{2+} ion in octahedral (O_h)

Table 2 ^1H T_1 relaxation times of Co^{2+}-doped $MAPbI_3$ fitted using the mono-/bi-exponential function. The reported errors correspond to one standard deviation

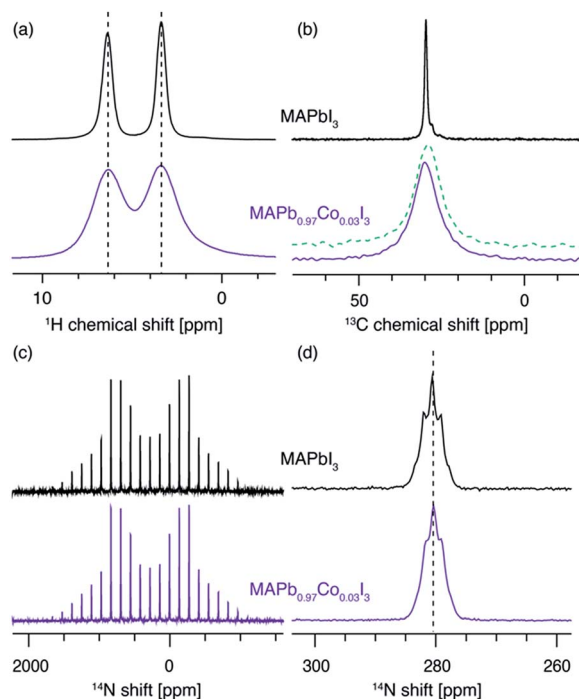| Material	$_1H$ T_1 [s]	
	Component 1	Component 2
$MAPbI_3$	15.89 ± 0.04	—
$MAPb_{0.97}Co_{0.03}I_3$	15.3 ± 0.2	—
$MAPb_{0.97}Co_{0.03}I_3$	15.89 (constraint)	0.01 ± 0.01
MA_2CoI_4	0.0067 ± 0.0001	—

Fig. 3 A comparison of (a) ^{1}H (20 kHz MAS, 11.7 T, 300 K), (b) ^{13}C (12.5 kHz MAS, 11.7 T, 100 K), (c) ^{14}N (5 kHz MAS, 11.7 T, 300 K) and (d) ^{14}N (20 kHz MAS, 11.7 T, 300 K) of MAPbI$_3$ and MAPb$_{0.97}$Co$_{0.03}$I$_3$. The green dashed line in panel (b) is a ^{13}C spectrum of MAPbI$_3$ lightly mixed with 3 mol% of CoI$_2$ acquired under identical conditions. The pronounced broadening is caused by bulk magnetic susceptibility effects.

Fig. 4 Spatial dependence of spin-lattice relaxation time T_1 in two neighbouring domains: $T_{1,cluster} = 23$ ms (CsMnBr$_3$), $T_{1,dia} = 108.5$ s (CsPbBr$_3$) lattice for a CsMnBr$_3$ cluster with a radius of (a) 4.8 nm and (b) 48 nm. (c) Simulated spatial dependence of polarisation in the two domains for a cluster with a radius of 4.8 nm. Experimental (blue circles) and simulated signal build-up (solid lines) as a function of the recovery delay for different cluster radii for (d) CsPb$_{0.995}$Mn$_{0.005}$Br$_3$, (e) CsPb$_{0.97}$Mn$_{0.03}$Br$_3$, (f) CsPb$_{0.92}$Mn$_{0.08}$Br$_3$.

symmetry, shifts on the order of 10 ppm are expected.[50,74,75] For example, the H–Co^{2+} distance of about 3.5 angstroms[76] in the MA$_2$CoI$_4$ paramagnetic reference phase leads to an isotropic ^{1}H shift of 24.7 ppm (Fig. S5,† a relative shift of about 20 ppm compared to the diamagnetic MAPbI$_3$). We have previously shown that ^{14}N spectral envelopes are a sensitive probe of cation incorporation into perovskites, as they indicate changes in the symmetry of the cubooctahedral cavity in which the picosecond time scale cation reorientation takes place.[43–45] The ^{14}N spectral envelopes of both materials are identical, indicating that the reorientation symmetry of the MA cation did not change upon Co^{2+} doping, consistent with no change in the crystallographic symmetry of the main perovskite phase (Fig. 3c). The significant broadening present in the sample doped with Co^{2+} is due to bulk magnetic susceptibility effects caused by the presence of a secondary paramagnetic phase leading to inhomogeneity of the magnetic field inside the sample volume.[77,78] This effect can be reproduced by simply mixing MAPbI$_3$ with 3 mol% of CoI$_2$, *without* mechanochemical grinding and annealing (Fig. 3b, green dashed line). Notably, beside pronounced broadening, bulk magnetic susceptibility effects can also cause small shifts, depending on the homogeneity of mixing of the two phases. These shifts can potentially be misinterpreted as a change in the underlying molecular structure. This effect is also visible here (Fig. 3b, green dashed line *vs.* violet solid line) and it highlights the key advantage of the relaxation-based methodology. No EPR spectra could be detected from MAPbI$_3$ doped

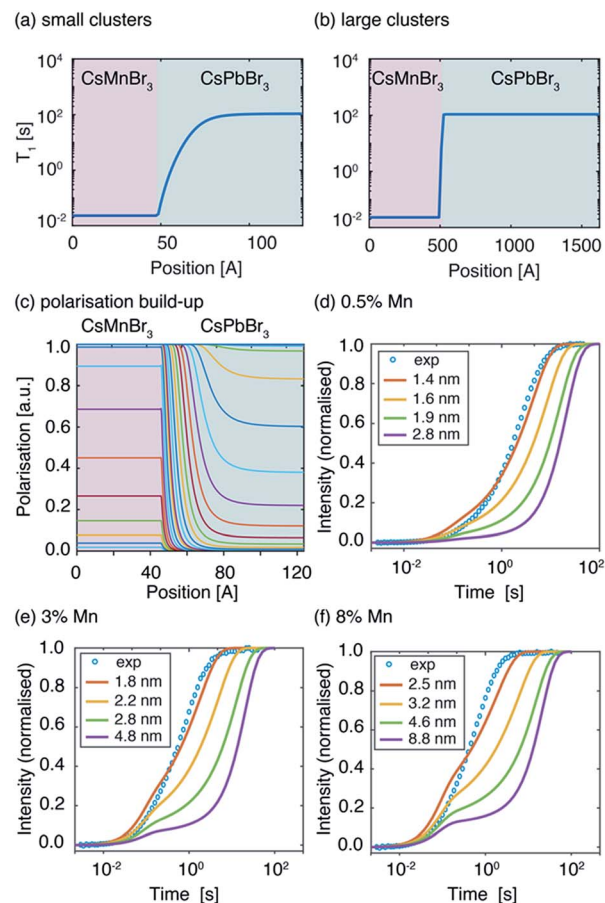with Co^{2+} and MA$_2$CoI$_4$, consistent with the very large exchange interaction expected in cobalt-rich phases. The XRD patterns of the materials are shown in Fig. S3.† All these observations are thus consistent with no incorporation of Co^{2+} into the perovskite lattice.

In order to further probe Mn^{2+} aggregation inside the perovskite lattice, we modelled the spatial distribution of polarisation in the presence of Mn-induced PRE by describing polarisation dynamics using a heat transfer equation.[51] The full procedure is described in the SI. As described in the introduction, the PRE effect can in some cases propagate through spin diffusion. We use a pseudopotential defined by De Gennes[79] to describe the competition between PRE and SD and demonstrate that in the case of Mn-doped CsPbBr$_3$ the PRE effect is not relayed by spin diffusion (see the ESI† for full derivation). To model domain formation, we consider spherical clusters of CsMnBr$_3$ surrounded by a CsPbBr$_3$ lattice. Inside the cluster, the ^{133}Cs spin-lattice relaxation time was measured to be $T_{1,cluster} = 23$ ms. Outside the cluster, the ^{133}Cs T_1 depends on

2330 | *J. Mater. Chem. A*, 2019, **7**, 2326–2333

This journal is © The Royal Society of Chemistry 2019

the distance between the cesium atom and the nearest manganese atom from the CsMnBr$_3$ cluster and follows an r^{-6} dependence. We consider paramagnetic clusters with a radius of between 1.4 and 8.8 nm, schematically shown in Fig. 4a and b.

The resulting polarisation dynamics can then be plotted as a function of position, for different time steps in a saturation recovery experiment (Fig. 4c). As expected, the polarisation is predicted to build up quickly inside the CsMnBr$_3$ region due to strong PRE, and more slowly in the diamagnetic CsPbBr$_3$ region. The simulation is then performed for increasing cluster radii while adjusting the diamagnetic volume so that the doping percentage is respected. The build-up curves obtained in this way are shown in Fig. 4d–f. For the largest cluster radii, the simulated build-up behaviour is clearly bi-exponential. By fitting the curves one obtains a component corresponding to cesium atoms located inside the paramagnetic cluster with a $T_{1,fit} = 23$ ms and representing 0.5%, 3%, and 8% of the total build-up, while the second component represents 99.5%, 97%, and 92%, respectively, of the total build-up with a $T_{1,fit} = 108$ s. These results demonstrate that for large clusters, the PRE effect in the diamagnetic CsPbBr$_3$ lattice is negligible given the comparatively low surface area of the cluster. However, as the radius of the paramagnetic cluster decreases, the surface area increases and the PRE effect in the diamagnetic part of the lattice becomes more pronounced, leading to stretched exponential behaviour. *Comparing this simulation with the experimental curves allows us to conclude that the manganese dopant does not form manganese-rich clusters larger than 1.6 nm (2 unit cells), 2.2 nm (3 unit cells), and 3.2 nm (5 unit cells) for 0.5%, 3% and 8% Mn^{2+} doping, respectively.* Finally, we note that the numerical simulation does not perfectly reproduce the experimentally observed recovery curve. This is caused by the fact that the simulation, based on the heat transfer equation, describes the flow of polarization in the spin system as being continuous. In reality, the lattice is composed of discrete unit cells which renders this approach approximate when the involved length scale is on the order of the lattice parameters, as it is the case here for the smallest clusters. Finally, we note that this approach yields information on the cluster size but not the homogeneity or spatial distribution of the clusters.

Conclusions

In conclusion, we have shown that the introduction of paramagnetic dopants into perovskite phases leads to substantial shortening of their nuclear relaxation times. This approach is a straightforward and general method for evidencing substitutional doping of perovskites with paramagnetic transition metal or lanthanide ions. Specifically, we have shown that Mn^{2+} is readily incorporated into CsPbBr$_3$ and CsPbCl$_3$ up to at least 8 mol% and 3%, respectively and that if it forms any clusters they are not larger than 2 to 5 unit cells, depending on the doping level. Conversely, we show that Co^{2+} is not capable of doping the MAPbI$_3$ perovskite phase. We believe that this simple, relaxation-based approach should become a routine tool for the characterization of perovskites doped with paramagnetic ions.

Conflicts of interest

There are no conflicts to declare.

Acknowledgements

Notes and references

1 W. Li, Z. Wang, F. Deschler, S. Gao, R. H. Friend and A. K. Cheetham, *Nat. Rev. Mater.*, 2017, **2**, 16099.

2 L. Protesescu, S. Yakunin, M. I. Bodnarchuk, F. Krieg, R. Caputo, C. H. Hendon, R. X. Yang, A. Walsh and M. V. Kovalenko, *Nano Lett.*, 2015, **15**, 3692–3696.

3 G. Nedelcu, L. Protesescu, S. Yakunin, M. I. Bodnarchuk, M. J. Grotevent and M. V. Kovalenko, *Nano Lett.*, 2015, **15**, 5635–5640.

4 Q. A. Akkerman, V. D'Innocenzo, S. Accornero, A. Scarpellini, A. Petrozza, M. Prato and L. Manna, *J. Am. Chem. Soc.*, 2015, **137**, 10276–10281.

5 S. Sun, D. Yuan, Y. Xu, A. Wang and Z. Deng, *ACS Nano*, 2016, **10**, 3648–3657.

6 D. Zhang, S. W. Eaton, Y. Yu, L. Dou and P. Yang, *J. Am. Chem. Soc.*, 2015, **137**, 9230–9233.

7 A. Kojima, K. Teshima, Y. Shirai and T. Miyasaka, *J. Am. Chem. Soc.*, 2009, **131**, 6050–6051.

8 W. S. Yang, B.-W. Park, E. H. Jung, N. J. Jeon, Y. C. Kim, D. U. Lee, S. S. Shin, J. Seo, E. K. Kim, J. H. Noh and S. I. Seok, *Science*, 2017, **356**, 1376–1379.

9 W. Liu, Q. Lin, H. Li, K. Wu, I. Robel, J. M. Pietryga and V. I. Klimov, *J. Am. Chem. Soc.*, 2016, **138**, 14954–14961.

10 D. Parobek, B. J. Roman, Y. Dong, H. Jin, E. Lee, M. Sheldon and D. H. Son, *Nano Lett.*, 2016, **16**, 7376–7380.

11 S. Zou, Y. Liu, J. Li, C. Liu, R. Feng, F. Jiang, Y. Li, J. Song, H. Zeng, M. Hong and X. Chen, *J. Am. Chem. Soc.*, 2017, **139**, 11443–11450.

12 Q. A. Akkerman, D. Meggiolaro, Z. Dang, F. De Angelis and L. Manna, *ACS Energy Lett.*, 2017, **2**, 2183–2186.

13 K. Xu, C. C. Lin, X. Xie and A. Meijerink, *Chem. Mater.*, 2017, **29**, 4265–4272.

14 X. Yuan, S. Ji, M. C. De Siena, L. Fei, Z. Zhao, Y. Wang, H. Li, J. Zhao and D. R. Gamelin, *Chem. Mater.*, 2017, **29**, 8003–8011.

This journal is © The Royal Society of Chemistry 2019

J. Mater. Chem. A, 2019, **7**, 2326–2333 | 2331

15 D. Rossi, D. Parobek, Y. Dong and D. H. Son, *J. Phys. Chem. C*, 2017, **121**, 17143–17149.

16 D. Gao, B. Qiao, Z. Xu, D. Song, P. Song, Z. Liang, Z. Shen, J. Cao, J. Zhang and S. Zhao, *J. Phys. Chem. C*, 2017, **121**, 20387–20395.

17 J. Zhu, X. Yang, Y. Zhu, Y. Wang, J. Cai, J. Shen, L. Sun and C. Li, *J. Phys. Chem. Lett.*, 2017, **8**, 4167–4171.

18 W. J. Mir, M. Jagadeeswararao, S. Das and A. Nag, *ACS Energy Lett.*, 2017, **2**, 537–543.

19 Q. Wang, X. Zhang, Z. Jin, J. Zhang, Z. Gao, Y. Li and S. F. Liu, *ACS Energy Lett.*, 2017, **2**, 1479–1486.

20 F. Meinardi, Q. A. Akkerman, F. Bruni, S. Park, M. Mauri, Z. Dang, L. Manna and S. Brovelli, *ACS Energy Lett.*, 2017, **2**, 2368–2377.

21 H. Liu, Z. Wu, J. Shao, D. Yao, H. Gao, Y. Liu, W. Yu, H. Zhang and B. Yang, *ACS Nano*, 2017, **11**, 2239–2247.

22 T. He, J. Li, C. Ren, S. Xiao, Y. Li, R. Chen and X. Lin, *Appl. Phys. Lett.*, 2017, **111**, 211105/1–211105/4.

23 J.-H. Cha, J. H. Han, W. Yin, C. Park, Y. Park, T. K. Ahn, J. H. Cho and D.-Y. Jung, *J. Phys. Chem. Lett.*, 2017, **8**, 565–570.

24 M. Lorenzon, L. Sortino, Q. Akkerman, S. Accornero, J. Pedrini, M. Prato, V. Pinchetti, F. Meinardi, L. Manna and S. Brovelli, *Nano Lett.*, 2017, **17**, 3844–3853.

25 C. Zhou, Y. Tian, O. Khabou, M. Worku, Y. Zhou, J. Hurley, H. Lin and B. Ma, *ACS Appl. Mater. Interfaces*, 2017, **9**, 40446–40451.

26 D. Parobek, Y. Dong, T. Qiao and D. H. Son, *Chem. Mater.*, 2018, **30**, 2939–2944.

27 D. Chen, G. Fang and X. Chen, *ACS Appl. Mater. Interfaces*, 2017, **9**, 40477–40487.

28 H. Wu, S. Xu, H. Shao, L. Li, Y. Cui and C. Wang, *Nanoscale*, 2017, **9**, 16858–16863.

29 P. Wang, B. Dong, Z. Cui, R. Gao, G. Su, W. Wang and L. Cao, *RSC Adv.*, 2018, **8**, 1940–1947.

30 J.-S. Yao, J. Ge, B.-N. Han, K.-H. Wang, H.-B. Yao, H.-L. Yu, J.-H. Li, B.-S. Zhu, J.-Z. Song, C. Chen, Q. Zhang, H.-B. Zeng, Y. Luo and S.-H. Yu, *J. Am. Chem. Soc.*, 2018, **140**, 3626–3634.

31 M. T. Klug, A. Osherov, A. A. Haghighirad, S. D. Stranks, P. R. Brown, S. Bai, J. T.-W. Wang, X. Dang, V. Bulovic, H. J. Snaith and A. M. Belcher, *Energy Environ. Sci.*, 2017, **10**, 236–246.

32 S. T. Williams, A. Rajagopal, S. B. Jo, C.-C. Chueh, T. F. L. Tang, A. Kraeger and A. K.-Y. Jen, *J. Mater. Chem. A*, 2017, **5**, 10640–10650.

33 R. Beaulac, P. I. Archer, J. van Rijssel, A. Meijerink and D. R. Gamelin, *Nano Lett.*, 2008, **8**, 2949–2953.

34 S. Kondo, K. Amaya and T. Saito, *Journal of Physics-Condensed Matter*, 2002, **14**, 2093–2099.

35 K. -H. Wang, L. Wu, L. Lei, H. -B. Yao, H. -S. Qian and S. -H. Yu, *Angew. Chem., Int. Ed.*, 2016, **55**, 8328–8332.

36 Q. A. Akkerman, S. Park, E. Radicchi, F. Nunzi, E. Mosconi, F. De Angelis, R. Brescia, P. Rastogi, M. Prato and L. Manna, *Nano Lett.*, 2017, **17**, 1924–1930.

37 O. Knop, R. E. Wasylishen, M. A. White, T. S. Cameron and M. J. M. Van Oort, *Can. J. Chem.*, 1990, **68**, 412–422.

38 B. A. Rosales, L. Men, S. D. Cady, M. P. Hanrahan, A. J. Rossini and J. Vela, *Chem. Mater.*, 2016, **28**, 6848–6859.

39 B. A. Rosales, M. P. Hanrahan, B. W. Boote, A. J. Rossini, E. A. Smith and J. Vela, *ACS Energy Lett.*, 2017, **2**, 906–914.

40 C. Roiland, G. Trippe-Allard, K. Jemli, B. Alonso, J.-C. Ameline, R. Gautier, T. Bataille, L. Le Polles, E. Deleporte, J. Even and C. Katan, *Phys. Chem. Chem. Phys.*, 2016, **18**, 27133–27142.

41 W. M. J. Franssen, S. G. D. van Es, R. Dervisoglu, G. A. de Wijs and A. P. M. Kentgens, *J. Phys. Chem. Lett.*, 2017, **8**, 61–66.

42 A. Senocrate, I. Moudrakovski, G. Y. Kim, T.-Y. Yang, G. Gregori, M. Grätzel and J. Maier, *Angew. Chem., Int. Ed.*, 2017, **56**, 7755–7759.

43 D. J. Kubicki, D. Prochowicz, A. Hofstetter, P. Péchy, S. M. Zakeeruddin, M. Grätzel and L. Emsley, *J. Am. Chem. Soc.*, 2017, **139**, 10055–10061.

44 D. J. Kubicki, D. Prochowicz, A. Hofstetter, S. M. Zakeeruddin, M. Grätzel and L. Emsley, *J. Am. Chem. Soc.*, 2017, **139**, 14173–14180.

45 D. J. Kubicki, D. Prochowicz, A. Hofstetter, M. Saski, P. Yadav, D. Bi, N. Pellet, J. Lewiński, S. M. Zakeeruddin, M. Grätzel and L. Emsley, *J. Am. Chem. Soc.*, 2018, **140**, 3345–3351.

46 D. J. Kubicki, D. Prochowicz, A. Hofstetter, S. M. Zakeeruddin, M. Grätzel and L. Emsley, *J. Am. Chem. Soc.*, 2018, **140**, 7232–7238.

47 A. Karmakar, A. M. Askar, G. M. Bernard, V. V. Terskikh, M. Ha, S. Patel, K. Shankar and V. K. Michaelis, *Chem. Mater.*, 2018, **30**, 2309–2321.

48 T. Polenova, R. Gupta and A. Goldbourt, *Anal. Chem.*, 2015, **87**, 5458–5469.

49 I. Solomon, *Phys. Rev.*, 1955, **99**, 559–565.

50 I. Bertini, C. Luchinat, G. Parigi and E. Ravera, *NMR of Paramagnetic Molecules*, Elsevier Science, 2017.

51 N. Bloembergen, *Physica*, 1949, **15**, 386–426.

52 S. Hayashi and K. Hayamizu, *Bull. Chem. Soc. Jpn.*, 1990, **63**, 913–919.

53 D. Prochowicz, M. Franckevicius, A. M. Cieslak, S. M. Zakeeruddin, M. Gratzel and J. Lewinski, *J. Mater. Chem. A*, 2015, **3**, 20772–20777.

54 D. Prochowicz, P. Yadav, M. Saliba, M. Saski, S. M. Zakeeruddin, J. Lewinski and M. Gratzel, *Sustainable Energy Fuels*, 2017, **1**, 689–693.

55 M. GORDON and M. HOCH, *Journal of Physics C-Solid State Physics*, 1978, **11**, 783–795.

56 W. E. Blumberg, *Phys. Rev.*, 1960, **119**, 79–84.

57 I. J. Lowe and D. Tse, *Phys. Rev.*, 1968, **166**, 279–291.

58 D. Tse and S. R. Hartmann, *Phys. Rev. Lett.*, 1968, **21**, 511–514.

59 P. M. Henrichs, M. Linder and J. M. Hewitt, *J. Chem. Phys.*, 1986, **85**, 7077–7086.

60 A. Narayanan, J. S. Hartman and A. D. Bain, *J. Magn. Reson., Ser. A*, 1995, **112**, 58–65.

61 M. H. Alaimo and I. E. Roberts, *Solid State Nucl. Magn. Reson.*, 1997, **8**, 241–250.

2332 | *J. Mater. Chem. A*, 2019, **7**, 2326–2333

This journal is © The Royal Society of Chemistry 2019

62 J. S. Hartman, A. Narayanan and Y. Wang, *J. Am. Chem. Soc.*, 1994, **116**, 4019–4027.

63 H. -J. Seifert and E. Dau, *Z. Anorg. Allg. Chem.*, 1972, **391**, 302–312.

64 K. Keller, M. Zalibera, M. Qi, V. Koch, J. Wegner, H. Hintz, A. Godt, G. Jeschke, A. Savitsky and M. Yulikov, *Phys. Chem. Chem. Phys.*, 2016, **18**, 25120–25135.

65 R. E. Taylor, P. A. Beckmann, S. Bai and C. Dybowski, *J. Phys. Chem. C*, 2014, **118**, 9143–9153.

66 Q. Xu, E. Taro, H. Nakayama, N. Nakamura and K. Michihiko, *Z. Naturforsch.*, 2014, **46**, 240.

67 A. Senocrate, I. Moudrakovski and J. Maier, *Phys. Chem. Chem. Phys.*, 2018, **20**, 20043–20055.

68 D. L. Bryce, G. D. Sward and S. Adiga, *J. Am. Chem. Soc.*, 2006, **128**, 2121–2134.

69 C. M. Widdifield, R. P. Chapman and D. L. Bryce, in *Annual Reports on NMR Spectroscopy*, Academic Press, 2009, vol. 66, pp. 195–326.

70 C. M. Widdifield and D. L. Bryce, *J. Phys. Chem. A*, 2010, **114**, 10810–10823.

71 C. Marichal, J. Hirschinger, P. Granger, M. Menetrier, A. Rougier and C. Delmas, *Inorg. Chem.*, 1995, **34**, 1773–1778.

72 V. Ladizhansky and S. Vega, *J. Phys. Chem. B*, 2000, **104**, 5237–5241.

73 A. J. Pell, G. Pintacuda and C. P. Grey, *Prog. Nucl. Magn. Reson. Spectrosc.*, DOI: 10.1016/j.pnmrs.2018.05.001.

74 S. Balayssac, I. Bertini, M. Lelli, C. Luchinat and M. Maletta, *J. Am. Chem. Soc.*, 2007, **129**, 2218–2219.

75 I. Bertini, A. Bhaumik, G. De Paëpe, R. G. Griffin, M. Lelli, J. R. Lewandowski and C. Luchinat, *J. Am. Chem. Soc.*, 2010, **132**, 1032–1040.

76 M. Daub, R. Stroh and H. Harald, *Z. Anorg. Allg. Chem.*, 2016, **642**, 268–274.

77 N. Bloembergen and W. C. Dickinson, *Phys. Rev.*, 1950, **79**, 179–180.

78 A. Kubo, T. P. Spaniol and T. Terao, *J. Magn. Reson.*, 1998, **133**, 330–340.

79 P.-G. de Gennes, *J. Phys. Chem. Solids*, 1958, **7**, 345–350.

This journal is © The Royal Society of Chemistry 2019

J. Mater. Chem. A, 2019, **7**, 2326–2333 | **2333**